APPLIED SCIENCES AND ENGINEERING

Bioprinted optoelectronically active cardiac tissues

Faheem Ershad[1,2,3]†, Zhoulyu Rao[4,5]†, Sushila Maharajan[6]†, Fernanda C. Paccola Mesquita[7], Junkyu Ha[2,3,8], Lei Gonzalez[9], Tahir Haideri[3], Ernesto Curty da Costa[7], Angel Moctezuma-Ramirez[10], Yuqi Wang[3], Seonmin Jang[4], Yuntao Lu[4], Shubham Patel[4,5], Xiaoyang Wang[4,5,11], Yifan Tao[5], Joshua Weygant[6], Carlos Ezio Garciamendez-Mijares[6], Luis Carlos Orrantia Clark[6], Muhammad Zubair[3,4], Xiaojun Lance Lian[3], Abdelmotagaly Elgalad[10], Jian Yang[12], Camila Hochman-Mendez[7], Yu Shrike Zhang[6]*, Cunjiang Yu[1,2,3,4,5,8,11,13,14]*

Electrical stimulation of existing three-dimensional bioprinted tissues to alter tissue activities is typically associated with wired delivery, invasive electrode placement, and potential cell damage, minimizing its efficacy in cardiac modulation. Here, we report an optoelectronically active scaffold based on printed gelatin methacryloyl embedded with micro-solar cells, seeded with cardiomyocytes to form light-stimulable tissues. This enables untethered, noninvasive, and damage-free optoelectronic stimulation–induced modulation of cardiac beating behaviors without needing wires or genetic modifications to the tissue solely with light. Pulsed light stimulation of human cardiomyocytes showed that the optoelectronically active scaffold could increase their beating rates (>40%), maintain high cell viability under light stimulation (>96%), and negligibly affect the electrocardiogram morphology. The seeded scaffolds, termed optoelectronically active tissues, were able to successfully accelerate heart beating in vivo in rats. Our work demonstrates a viable wireless, printable, and optically controllable tissue, suggesting a transformative step in future therapy of electrically active tissues/organs.

INTRODUCTION

Three-dimensional bioprinted tissues have emerged as a powerful and widespread tool to achieve cardiac tissue repair and therapy (*1*–*3*). Despite their similarities with the native myocardium, these constructs often lack the inherent capability to dynamically interact with the host tissues, limiting their therapeutic potential. Addressing this limitation, electrical modulation of beating behaviors in printed tissues becomes crucial, not only for pacing the constructs but also for ensuring their synchronized host integration. Traditionally, these printed tissues are a composite of cells and an extracellular matrix (ECM), lacking the intrinsic ability to generate electrical signals necessary for stimulating cellular activity. To compensate, external stimulation sources are essential. However, modulating the activity of printed and other engineered tissues relies on conventional means of electrical stimulation, with stimulators in formats such as planar electrodes (*4*), wires (*5*), and rods (*6*–*8*). These often necessitate wired setups and invasive electrode placement and can lead to local damage at the stimulation sites among other unintended side effects (*9*–*12*), unlike distributed stimulation approaches (*13*).

Here, we propose to integrate optoelectronic materials into bioprinted scaffolds, creating active, electrically generative, and light-responsive tissues that diverge from conventional passive engineered tissues. Electrically stimulable printed tissues in a tether-less format, without the need for sticking additional wires to the printed construct, could be a highly sought-after therapeutic approach as they can circumvent the challenges of conventional electrical stimulators and enhance the cellular activities. Specifically, our bioprinted optoelectronically active tissue platform enables untethered, noninvasive, and distributed modulation of cardiac tissues, applicable at the in vitro and in vivo scales. We created a gelatin methacryloyl (GelMA)–based ink mixed with micro-solar cells (μ-solar cells), printable into arbitrary anatomies to form a scaffold. Once printed, these scaffolds were seeded with the appropriate cell type and subsequently bonded on the target tissue surface for stimulation. We characterized the printing of μ-solar cells embedded in GelMA (termed optoelectronically active ink), followed by evaluating the effect of remote optoelectronic stimulation. Our investigations revealed the capability of distributed μ-solar cells to stimulate cardiomyocytes (CMs) effectively in vitro. Detailed biological assessments unveiled that the integrated CMs on the scaffolds, embedded with μ-solar cells, sustained their rhythmic contractions and consistently expressed cardiac-specific biomarkers. Excitingly, in vitro evaluations of our optoelectronically active scaffolds ascertained that, despite being encapsulated in the ink, the μ-solar cells retained their efficacy, synchronizing and accelerating the beating of both human CMs and rat CMs (rCMs) across multiple periods of untethered optoelectronic stimulation. Implantation of the optoelectronically active tissue on a rat heart, as a proof of concept, further portrayed that our hybrid-engineered tissue-electronics scaffold could modulate the beating of the living rat heart. It is pertinent to note that our approach avoids

---

[1]Department of Electrical and Computer Engineering, University of Illinois Urbana-Champaign, Urbana, IL 61801, USA. [2]Beckman Institute for Advanced Science and Technology, University of Illinois Urbana-Champaign, Urbana, IL 61801, USA. [3]Department of Biomedical Engineering, Pennsylvania State University, University Park, PA 16802, USA. [4]Materials Research Laboratory, University of Illinois Urbana-Champaign, Urbana, IL 61801, USA. [5]Department of Engineering Science and Mechanics, Pennsylvania State University, University Park, PA 16802, USA. [6]Division of Engineering in Medicine, Department of Medicine, Brigham and Women's Hospital, Harvard Medical School, Cambridge, MA 02139, USA. [7]Regenerative Medicine Research Lab, Texas Heart Institute, Houston, TX 77030, USA. [8]Department of Bioengineering, University of Illinois Urbana-Champaign, Urbana, IL 61801, USA. [9]Department of Biomedical Engineering, University of Houston, Houston, TX 77204, USA. [10]Center for Preclinical Surgical & Interventional Research, Section of Transplantation, Texas Heart Institute, Houston, TX 77030, USA. [11]Department of Materials Science and Engineering, University of Illinois Urbana-Champaign, Urbana, IL 61801, USA. [12]Department of Materials Science and Engineering, Research Center for Industries of the Future, Westlake University, Hangzhou, Zhejiang 310030, P.R. China. [13]Department of Mechanical Science and Engineering, University of Illinois Urbana-Champaign, Urbana, IL 61801, USA. [14]Nick Holonyak Micro and Nanotechnology Laboratory, University of Illinois Urbana-Champaign, Urbana, IL 61801, USA.
*Corresponding author. Email: yszhang@bwh.harvard.edu (Y.S.Z.); cunjiang@illinois.edu (C.Y.)

†These authors contributed equally to this work.

the complexities of genetic interventions usually implemented for optical stimulation (*14*). The development and systematic investigations of the optoelectronically active ink and engineered tissue in this work emphasize that this wireless, nongenetically modified, and optically controlled bioprinted construct is a paradigm-shifting engineered tissue platform, which can pave the way for untethered light stimulation, tissue regeneration, and host integration capabilities in cardiac therapy and beyond.

RESULTS

Optoelectronically active ink

We first printed the optoelectronically active ink (a composite of μ-solar cells and GelMA) into scaffolds with different structures and then seeded the printed scaffolds with CMs (Fig. 1A). The optoelectronically active ink was prepared as described in the Materials and Methods section. Briefly, the preparation involved mixing a photo-cross-linkable precursor solution of GelMA (7 wt %) (*15*–*17*) with a suspension of μ-solar cells. The μ-solar cells were prepared by typical microfabrication and lithography procedures as described in Materials and Methods. Images of exemplary printed structures demonstrating the distribution of μ-solar cells in the GelMA are shown in Fig. 1B and fig. S1A. In Fig. 1B, an example of a printed heart using the optoelectronically active ink consisting of the atria and ventricles is presented. As a potential application, this optoelectronically active scaffold could be used to replace damaged scar tissue (Fig. 1C) in the native myocardium and be modulated to restore normal beating to the heart. Movie S1 shows the printing process of the optoelectronically active ink. Studies of the printing nozzle size and μ-solar cell size effects on the μ-solar cell

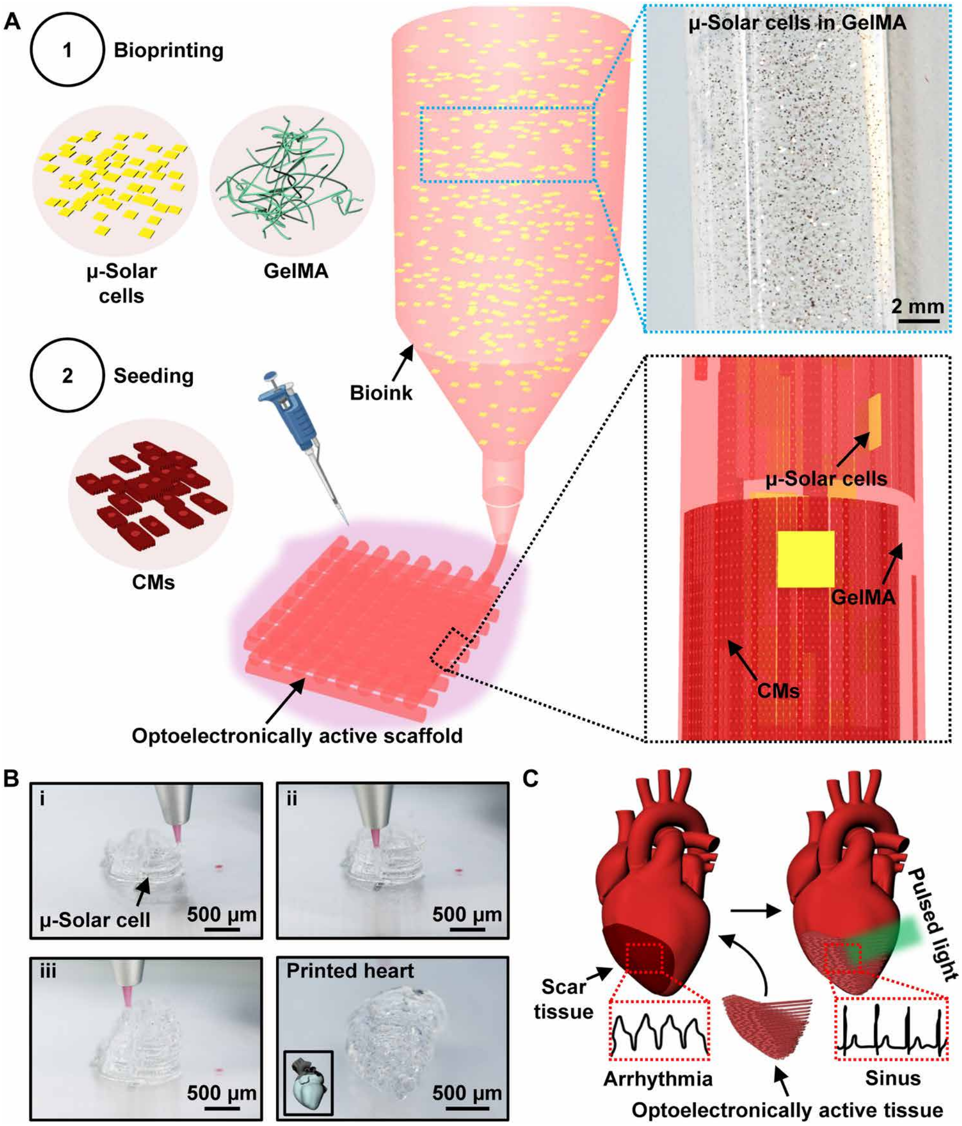

Fig. 1. Optoelectronically active bioink composition and printing. (**A**) Schematic of bioprinting combining μ-solar cells and GelMA and then seeding with CMs. (**B**) Photographs of the bioprinting process (i, ii, and iii) of the optoelectronic heart (atria and ventricles) along with a side view. Inset shows the model heart with the printed portion in blue and the remainder of the heart in gray. (**C**) Example of in vivo implantation of a printed optoelectronically active tissue and correction of arrhythmic beating.

distribution were performed to optimize the printing parameters and appropriate μ-solar cell size, as shown in fig. S1 (B to E). The density of the μ-solar cells solution was fixed to ~1300 μ-solar cells/ml as it was sufficient to modulate the beating rate of CMs, as evidenced in our later in vitro evaluations. From these studies, we determined the optimal printing conditions (line speed, bed/printhead temperatures, and extrusion pressure) using a 25-gauge (Ga) nozzle and 80-μm μ-solar cells as detailed in the Materials and Methods section. Investigations of the rheological properties (fig. S2, A to C) revealed that the uncross-linked optoelectronically active ink had a slightly higher storage/loss modulus (over different temperatures and oscillatory shear strains) and viscosity compared to pure GelMA (*18*). In fig. S2D, the cross-linked optoelectronically active ink showed a slightly lower modulus under compression (10.24 ± 2.33 kPa, means ± SD) compared to the control (16.59 ± 2.43 kPa, means ± SD) due to the presence of μ-solar cells, which likely prevented some cross-linking. Considering postprocessing analysis and eventual long-term evaluation, the in vitro swelling and degradation of the optoelectronically active ink were characterized in fig. S2 (E and F), respectively. After 6 hours, the swelling of the cross-linked GelMA and optoelectronically active ink increased by ~1000%. Both the cross-linked GelMA and optoelectronically active ink showed substantial degradation under an accelerated degradation test after 6 hours, reaching ~98 and ~88%, respectively. It is expected that the μ-solar cells would also degrade over a longer period and their degradation could be controlled by modifying their thickness (*19*). The by-products of the μ-solar cells when degraded (silicic acid) are known to be biocompatible. In addition, the absorbance and impedance of the optoelectronically active ink were determined to ensure that GelMA (before and after cross-linking) did not substantially hinder light penetration and the electrical potential distribution (fig. S2, G and H, respectively) produced by the μ-solar cells. Although cross-linking the optoelectronically active ink did decrease its transmittance, it was still relatively transparent. In addition, the Nyquist plot in fig. S2H shows that the addition of μ-solar cells had little effect on the impedance of the cross-linked ink. This finding verifies that the electric field generated by the μ-solar cells upon illumination would be minimally hindered.

μ-Solar cell characterization

Details of the μ-solar cells fabrication are in Materials and Methods and shown in fig. S3A. Briefly, the freestanding μ-solar cells were manufactured on a silicon wafer with a fabrication yield of ~100% (fig. S3B) and then collected by water-dissolvable tape (fig. S3C), followed by storing in a Dulbecco's phosphate-buffered saline (DPBS) solution in a vial after dissolving the tape (fig. S3D). The fabricated μ-solar cells exhibit a typical photovoltaic characteristic with an open-circuit voltage of ~0.5 V (fig. S3E). We then investigated the generated photocurrent by a single μ-solar cell using a patch-clamp setup (fig. S4A). Upon illumination with multiple 100-ms light pulses (532 nm), the μ-solar cell consistently produced ~3 nA in DPBS (Fig. 2, A to C, and fig. S4B). As a control, illuminating the pipette with the same parameters did not produce any artifacts as shown in fig. S4C. We next studied the effect of light stimulation, specifically subthreshold stimulation, in vitro.

Subthreshold stimulation, which has been shown to be effective for modulating the activity of neural (*20*, *21*) and cardiac cells (*22*–*24*), improves functional recovery after stroke (*25*) and prevents/treats ventricular tachycardia (*26*, *27*). To study the effect of subthreshold optoelectronic stimulation, we cocultured human-induced pluripotent stem cell–derived CMs (hiPSC-CMs) with the μ-solar cells. We first coated a multielectrode array (MEA) with fibronectin and then dispensed the μ-solar cell suspension onto the coated MEA. Afterward, hiPSC-CMs were seeded on top of the μ-solar cells. In Fig. 2D, an optical image of hiPSC-CMs cultured with μ-solar cells on an MEA is shown and the corresponding real-time beating rate of hiPSC-CMs under optoelectronic stimulation is plotted in Fig. 2E. It should be noted that the results are from hiPSC-CMs near a single representative channel of the MEA (n = 59 channels). The hiPSC-CMs had a spontaneous beating rate around 57 beats per minute (BPM) prior to any stimulation. The stimulation protocol (*22*) using light (532 nm, 100-ms pulse duration, 1.2 Hz, and ~2.8 mW/mm^2) is described in the following and illustrated in Fig. 2E. It is noted that, although this wavelength may not be sufficient to penetrate tissue as is, wavelengths in the near-infrared spectrum could be used or the tissue transparent window could be modified with dyes as well (*28*–*30*). We recorded the cardiac field potentials across the MEA during the prestimulation, stimulation, and poststimulation periods. It should be noted that no stimulation was applied during the pre- and post-stimulation periods. In total, we performed three rounds of the stimulation protocol where each round consisted of 1 min of recording during prestimulation, 10 min of stimulation, 1 min of recording during poststimulation, and 2 min of break. The target beating rate of 72 BPM was chosen based on the spontaneous beating rate and could be adjusted to the condition of the cultured cells (*22*). As evidenced by the BPM plot in Fig. 2E and the cardiac field potentials in Fig. 2F, the light stimulation protocol took ~40 min to accelerate the hiPSC-CMs to the target rate (26% increase from the initial beating rate). These results clearly demonstrated that the μ-solar cells and the appropriate untethered light stimulation protocol can be used to successfully accelerate the beating of the hiPSC-CMs. To verify the function of the μ-solar cells on the MEA without hiPSC-CMs, we illuminated a few μ-solar cells and they were shown to generate up to 1.5 mV (fig. S5, A to F). Additional evaluation following the same stimulation paradigm also was shown to be effective for primary rCMs as evidenced in fig. S6.

In vitro evaluation of the optoelectronically active scaffold

In subsequent experiments, we evaluated the biocompatibility of the optoelectronically active ink after printing it into a scaffold and seeding it with cells (Fig. 3A). The bright-field and fluorescence microscope images shown in Fig. 3 (B and C) for hiPSC-CMs and in fig. S7 (A and B) for rCMs seeded on the optoelectronically active scaffolds reveal the cytocompatibility of our materials. The cell viability remains high through the 2 weeks of maintenance (Fig. 3D). The confocal fluorescence microscopic images of hiPSC-CMs immunostained for sarcomeric α-actinin, connexin 43, cardiac troponin T, and cardiac troponin I on day 15 (Fig. 3, E and F) demonstrated the expression of these markers, along with the sarcomere patterns, indicating the structural maturation of hiPSC-CMs on the optoelectronically active scaffolds. The hiPSC-CMs show expected beating rates on days 7 and 15 (Fig. 3G). Similarly, the aforementioned markers were also expressed by rCMs seeded on optoelectronically active scaffolds (fig. S7, C and D). To ensure that light stimulation induced little to no harmful effect on the cells, we performed a phototoxicity assay. The results shown in Fig. 3 (H to L) and fig. S8 (A to C) reveal a negligible difference in cell viability (both >96%) between the stimulation-treated and untreated optoelectronically active scaffolds.

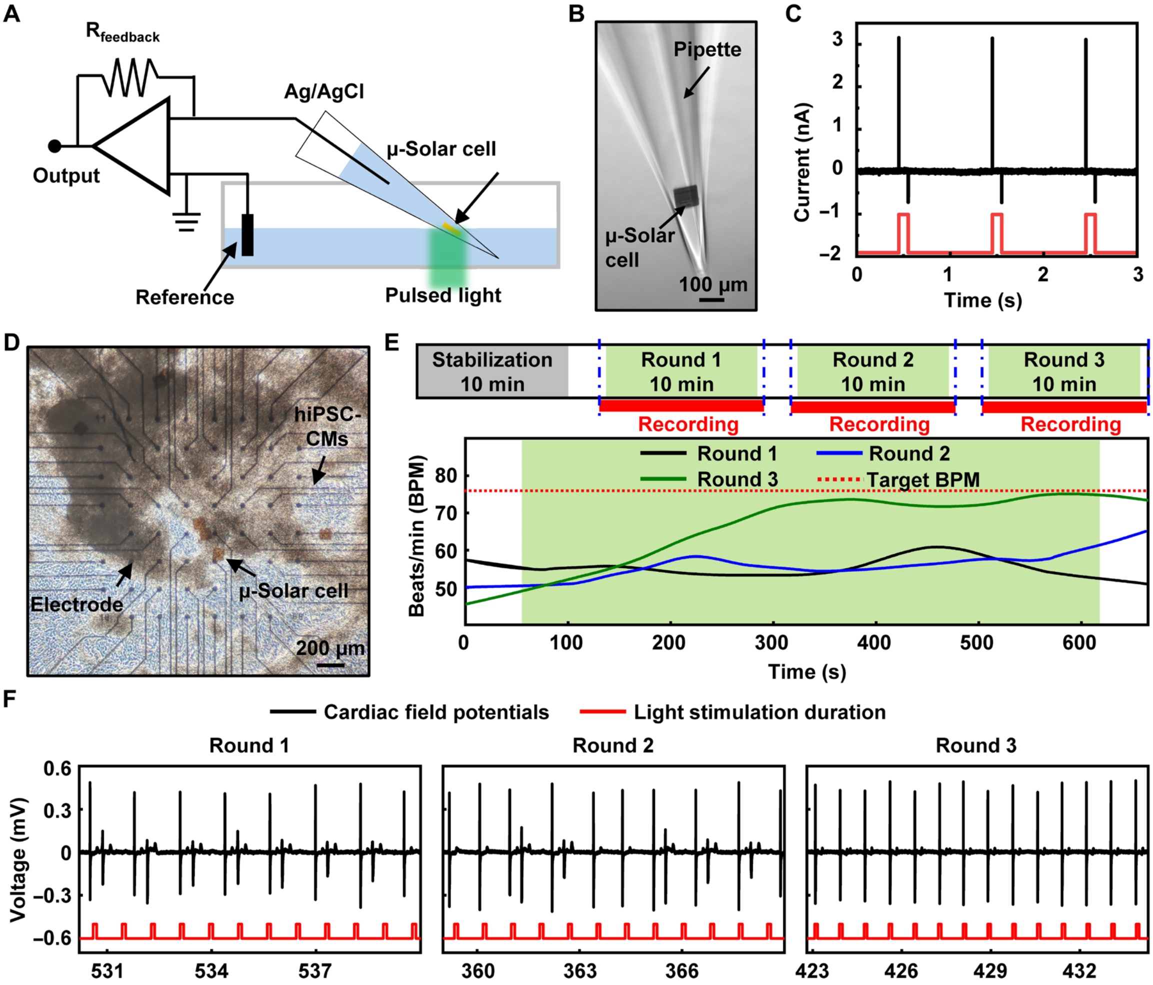

Fig. 2. μ-Solar cell characteristics and direct stimulation of CMs. (**A**) Schematic of patch-clamp measurements for the current amplitude of an individual μ-solar cell. (**B**) Microscope image of an individual μ-solar cell inside a patch pipette. (**C**) Current amplitudes recorded via patch clamp. (**D**) Microscope image of hiPSC-CMs seeded on an MEA plate containing μ-solar cells. (**E**) Optoelectronic subthreshold stimulation protocol (top) and beating rates of CMs after multiple rounds of stimulation at 1.2 Hz. (**F**) Cardiac field potentials shown from a representative channel of the MEA during the stimulation periods of each round.

We then evaluated the modulation capability of the optoelectronically active scaffold. To verify the function of an individual μ-solar cell in the optoelectronically active ink, again we used our patch-clamp setup. Results in fig. S9 (A to C) show the photocurrent generated by a single μ-solar cell in both uncross-linked and cross-linked GelMA; despite the slightly decreased transmittance after cross-linking the GelMA, a similar current level of ~2 nA could be observed in both cases, indicating that the absorption at our tested wavelength (532 nm) by the μ-solar cell was not hindered. As shown previously, no response was observed (fig. S9D) without the presence of a μ-solar cell inside the pipette. To evaluate the performance of many μ-solar cells in the optoelectronically active scaffolds, we prepared the scaffolds, seeded them with hiPSC-CMs, and then positioned them on MEA plates. The experimental setup is depicted in Fig. 4A. A photograph of the printed scaffold, embedded with μ-solar cells and seeded with hiPSC-CMs, is depicted in Fig. 4B along with its placement on an MEA plate (*n* = 59 channels) in Fig. 4C. A closer microscopic view is presented in Fig. 4D. Adhering to our previously established light stimulation protocol, we first stimulated hiPSC-CMs on the scaffold at a frequency of 1 Hz across four rounds. The resultant data revealed a BPM increase from an initial ~50 to ~60 BPM (20% increase). The RR (R-peak to R-peak) intervals during the four rounds for one representative channel are shown fig. S10. In the fourth round, the RR interval values are ~1 s. Transitioning to a stimulation frequency of 1.2 Hz for two subsequent rounds led to another increase in the beating rate, rising from ~60 to ~72 BPM. The CMs increased their beating rates by ~44% from the original ~50 BPM. This trend in beating rates across various channels, both pre- and post-stimulation, is graphically represented in Fig. 4E.

To emphasize the capability of the optoelectronically active scaffold for synchronizing and modulating the beating rate, we created activation heatmaps. As multiple rounds of stimulation progressed, the heatmaps showed shortened activation times, symbolized by a predominant blue hue across most of the channels. This observation is outlined in Fig. 4F, where the propagation time across the MEA decreased with each stimulation round. As expected, the changes in BPM from before to after stimulation (for each round) show a highly negative correlation with the RR intervals, especially in later

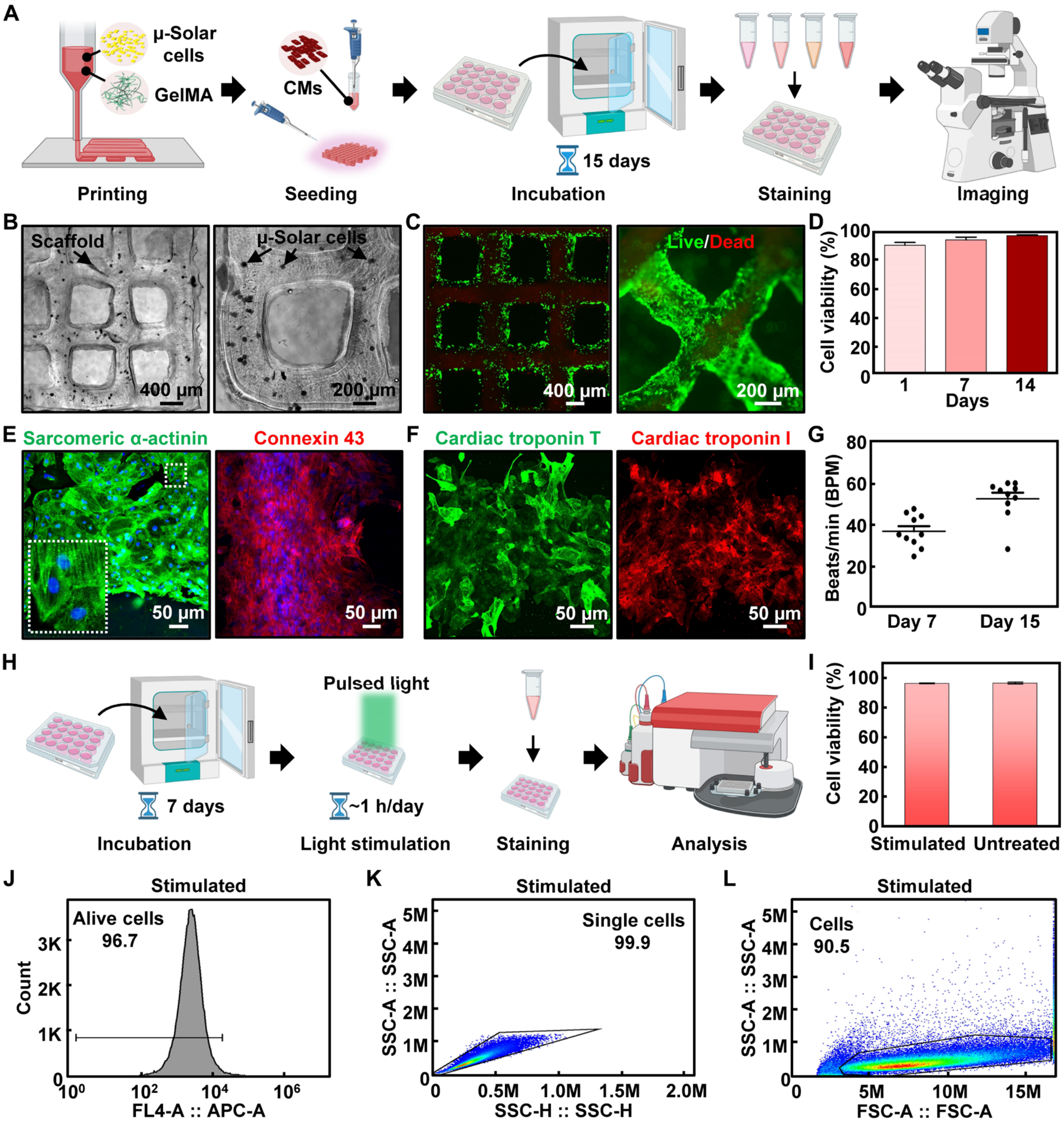

Fig. 3. CM viability and expression of cardiac markers on the optoelectronically active scaffold. (**A**) Schematic of scaffold fabrication, seeding, incubation, cell viability and immunostaining, and imaging. Made with BioRender.com. (**B**) Microscope images of an optoelectronically active scaffold seeded with CMs. (**C**) Live/dead image (left) and zoomed-in version (right) of CMs seeded on an optoelectronically active scaffold. Live cells are green, and dead cells are red. (**D**) Quantitative viability of CMs seeded on an optoelectronically active scaffold over multiple days. Data are presented as means ± SEM. (**E**) Fluorescence images of an optoelectronically active scaffold showing the expression of sarcomeric α-actinin (green) and presence of nuclei (blue) on the left and the expression of connexin 43 (red) and presence of nuclei (blue) on the right. (**F**) Fluorescence images (scale bars, 50 μm) of an optoelectronically active scaffold showing the expression of cardiac troponin T (green) and cardiac troponin I (red). (**G**) Beating rates of CMs on optoelectronically active scaffold without light stimulation over time. Data are presented as means ± SEM. (**H**) Schematic of light stimulation procedure and phototoxicity assay. Made with BioRender.com. h, hour. (**I**) Cell viability with and without stimulation of optoelectronically active scaffolds. Data are presented as means ± SEM. (**J**) Allophycocyanin (APC) fluorescence expression determined by flow cytometry. (**K**) Gating strategy used for excluding dead cells and subsequent doublet discrimination to exclude abnormal fluorescence events during flow cytometry. (**L**) Another gating strategy used for excluding dead cells and subsequent doublet discrimination.

rounds as shown in fig. S10. Movies S2 and S3 of another optoelectronically active scaffold visually reveal a clear acceleration in beating rate, before and after stimulation, respectively. One representative channel showing the changes in beating rate over time is shown in Fig. 4G. As expected, in the fourth round of stimulation, the CMs near this channel beat near the target rate of 60 BPM.

We also assessed the morphology of electrocardiogram (ECG) signals under subthreshold stimulation, focusing on parameters such as QRS duration, QR slope, RS slope, and peak-to-peak amplitude. Our results demonstrated that subthreshold stimulation did not induce significant changes in ECG wave morphology, as shown in fig. S11 (A to D). As a reference, fig. S12 (A and B) shows the points used to calculate

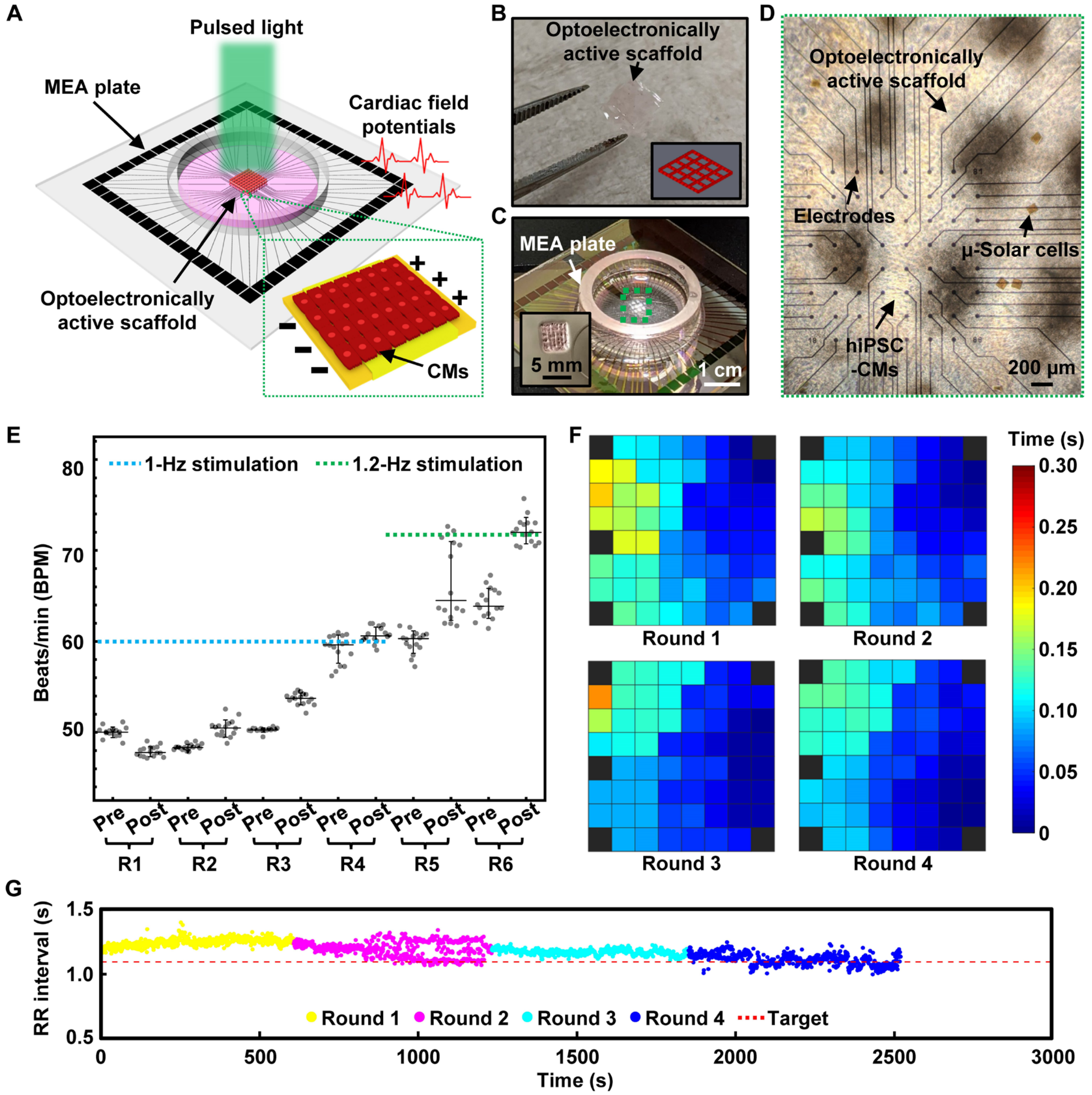

Fig. 4. Optoelectronically active scaffold evaluation in vitro. (**A**) Schematic of stimulating the optoelectronically active scaffold with light on an MEA plate. (**B**) Photograph of the printed optoelectronically active scaffold in media with the inset showing the model in a modeling program. (**C**) Photograph of the MEA plate containing the optoelectronically active scaffold. (**D**) Microscope image showing the optoelectronically active scaffold seeded with CMs. (**E**) Beating rates of CMs shown pre- and poststimulation for four rounds of stimulation at 1 Hz followed by two rounds of stimulation at 1.2 Hz. Horizontal lines + vertical lines indicate means ± SD ($n = 16$). (**F**) Activation maps of different rounds (poststimulation) during the 1-Hz stimulation periods. (**G**) RR interval values over time for a representative channel during four rounds of stimulation at 1 Hz. The yellow, magenta, cyan, and blue points represent RR intervals calculated for rounds 1, 2, 3, and 4, respectively. The red dashed line represents the target frequency ± tolerance level (0.1 s). The target frequency was 1 Hz, so the RR interval was expected to be 0.9 to 1.1 s.

ECG waveform parameters. The bar plots in fig. S13 (A to D) show that the P values were greater than 0.05 for nearly all channels among all the analyzed morphological features of the ECG signal. Our analysis shows that subthreshold stimulation does not significantly affect the QRS complex or other morphological features of ECG waves as it only mildly influences the electrophysiological behavior of CMs without inducing full action potentials. This finding is valuable as it underscores the potential of subthreshold stimulation for minimally invasive modulation of cardiac tissue without compromising the integrity of intrinsic electrical signaling (*12*). By maintaining the ECG morphology, the subthreshold approach also offers an advantage in therapies aimed at subtle cardiac modulation, supporting their role in applications where precise control without full excitation is desirable (*26*, *27*). In an additional experiment ($n = 59$ channels), we tested the upper limit at which the hiPSC-CMs could sustain the beating rate. Further limit testing for hiPSC-CMs shown in fig. S14 (A to C) reveal that they could only beat up to ~94 BPM (from initially around ~60 BPM, a 56% increase) despite being stimulated at 102 BPM (1.7 Hz). This could be attributed to the heterogeneity/inherent variability in baseline beating rates or a physiological limit for this population of cells (*23*).

In vivo evaluation of the optoelectronically active tissue

Integrating bioengineered cardiac constructs with the host tissue, specifically aligning their beating rates, is essential for successful host integration (*5*, *7*, *12*). Stimulating the engineered tissues to synchronize their beating with the host allows for the assembly of functional myocardium and reduces the potential for arrhythmia upon implantation. Last, in a proof-of-concept demonstration, we assessed the capability of the optoelectronically active tissue to accelerate the beating heart of a rat directly in vivo (Fig. 5A) to determine its potential for synchronization. Initially, the scaffold was constructed as outlined earlier and subsequently cultured with rCMs to form the optoelectronically active tissue. The rat was prepared in accordance with the methodologies detailed in the Materials and Methods section. Upon heart exposure and stabilization, the optoelectronically active tissue was delicately positioned and adhered on the epicardial surface above the right atrium, depicted in Fig. 5B. The initial heart rate was recorded at ~280 BPM, prompting us to select a target stimulation rate of ~5 Hz (~300 BPM). During the in vivo implantation, continuous light stimulation was applied until the target beating rate recorded from the rat heart was unambiguously observed. This heart rate progression is detailed in Fig. 5C. Over the stimulation interval, the heart rate gradually converged toward the target. The acquired ECG traces for each period (prestimulation, stimulation, and poststimulation) are shown in Fig. 5D. Before initiating stimulation, the heart rate stood at around 280 BPM. Roughly 12 min after the stimulation at ~5 Hz began, the ECG signals showed a heart rate nearing 302 BPM (7.8% increase from the initial beating rate). Once this target rate was sustained for a brief duration, the light stimulation was halted. Shortly, within ~3 min, the heart rate began to recede, settling close to 290 BPM. These findings underscore the capability of the printed optoelectronically active tissue for remote, light-driven, in situ modulation of the beating characteristics of a heart. Given the limited duration of this proof-of-concept experiment, the observed accelerated beating rate could likely be attributed to the μ-solar cells rather than the seeded rCMs, which would require more time to form connections to the host tissue. Control conditions (fig. S15) revealed that without the presence of μ-solar cells in the tissue (printed GelMA only, seeded with rCMs), the heart rate of another rat heart (initial rate of ~380 BPM) did not increase when stimulated at ~6.5 Hz (390 BPM). We further verified that change in temperature on the tissue surface during light stimulation did not play a substantial role in the successful modulation, as indicated in fig. S16 and movie S4. The slightly higher temperature increase after stimulation could be attributed to the accumulated heat at the end of each light pulse. With future longer-term studies, the tissue regeneration and host integration potential could be clarified. It is also noted that, although the current experiments were performed in an acute, open-chest surgery setting, using red or near-infrared light (*31*) could enable penetration through the tissue for closed-chest, chronic modulation. Our optoelectronically active tissues provide a dynamic, controllable platform that allows for light-stimulated modulation of beating rates. This approach not only enables potential matching of the beating rate of the implanted tissue with the host heart rate but could also offer noninvasive, bidirectional control, which is critical for both acute and long-term integration.

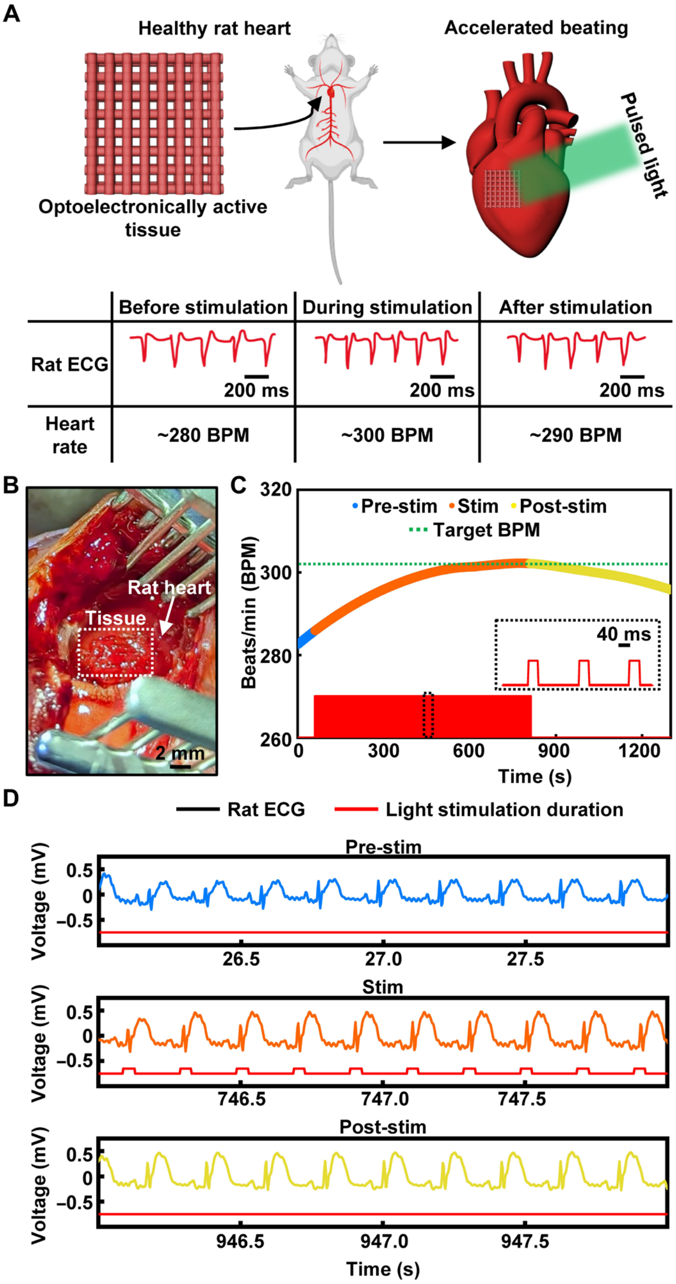

Fig. 5. Optoelectronically active tissue evaluation on a live rat heart. (**A**) Schematic showing the optoelectronically active tissue being used to accelerate the living rat heart. Figure made with BioRender.com. (**B**) Photograph of the optoelectronically active tissue on the rat heart surface. (**C**) Beating rates of the rat heart after stimulating at ~5 Hz. Inset shows the pulse duration. (**D**) ECG signals recorded from the rat during the prestimulation, stimulation, and poststimulation periods.

DISCUSSION

Although the existing bioprinted cardiac tissues have shown some efficacy for cardiac therapy, they are inherently passive and rely on tethered electrical stimulation to modulate their activity. Our approach has validated the optoelectronically active, bioprinted scaffolds and tissues for modulating the beating rates of hiPSC-CMs in vitro and in vivo rat hearts, without genetic intervention or need for wiring. The promise of our optoelectronically active tissues lies not only in their modulation capabilities but also in their prospective role in synchronizing implanted tissues with the cardiac rhythm of the host heart. Beyond the current proof-of-concept technology demonstrations, our future efforts will involve coprinting of CMs with the optoelectronically active ink, exploration of the long-term regenerative capability, and seamless integration of the optoelectronically active tissue within the host biology. It is noted that the materials that comprise our optoelectronically active scaffolds are not expected to produce acute nor long-term cardiac injury given that they have found wide usage in cardiac tissue engineering and interfacing (*1*, *19*). Furthermore, to enable applications in larger animal models and humans, other wavelengths (e.g., near infrared) or dyes could be used to match or modify the tissue transparent window for deeper penetration of light to the optoelectronically active tissues (*28*–*30*). The optoelectronically active tissues could also be scaled up with more printed layers and vascularization. The bioprinted, active tissues developed in this work signify a substantial shift from traditional passive tissue constructs to dynamic, responsive systems that could transform therapeutic strategies across electrically active tissues, including neural and muscle tissues. This fusion of soft biomaterials with embedded electronic functionalities stands poised to open new horizons in implantable therapeutic devices, tissue engineering, and personalized medicine.

MATERIALS AND METHODS

Fabrication of μ-solar cells

The ultrathin Si μ-solar cells were fabricated using a previously reported method (*32*, *33*). The processes began with selectively doping a silicon-on-insulator wafer (1250-nm-thick top Si layer, Soitec, Isere, France) to define planar P-I-N junctions. The top device layer was then isolated into squares using photolithography processes to form individual micrometer-sized particles. The sizes of the μ-solar cells were determined by a photomask designed using a maskless mask aligner (μMLA Maskless Aligner, Heidelberg Instruments Mikrotechnik GmbH, Heidelberg, Germany) and the AutoCAD software (Autodesk Inc., San Francisco, CA, USA). After releasing from the bulk substrate by removing the buried oxide layer in hydrofluoric acid, the μ-solar cells were picked up with water-dissolvable tape (fig. S3C). Finally, the μ-solar cells were collected for further studies after dissolving the tape in DPBS (Sigma-Aldrich, St. Louis, MO, USA; fig. S3D).

Preparation of the optoelectronically active ink

GelMA was synthesized according to the previously described protocol (*17*, *34*). Briefly, 10 g of type-A gelatin from the porcine skin was dissolved in 100 ml of DPBS at 50°C under constant stirring for 30 min. Next, 5.0 ml of methacrylic anhydride was then added to the gelatin solution dropwise and the reaction was carried out at 50°C. After 3 hours, the reaction was quenched by adding 100 ml of warm DPBS, followed by the dialysis of the product against distilled water at 40°C for 5 days using a dialysis membrane (molecular weight cutoff: 12,000 to 14,000 Da). The dialyzed GelMA solution was then filtered through a 0.2-μm filter and lyophilized to obtain porous white foam. GelMA was stored at −20°C until use. The optoelectronically active ink was prepared by first making a solution of a GelMA-precursor solution, which also consisted of lithium phenyl-2,4,6-trimethylbenzoylphosphinate (LAP; Sigma-Aldrich, St. Louis, MO, USA) and DPBS. A 7 wt % GelMA-precursor solution with 0.25 wt % LAP was prepared. The appropriate volume of DPBS was added after the μ-solar cell suspension (1300 μ-solar cells/ml) was mixed with the GelMA-precursor solution. The solution was then centrifuged in a conical tube at 300*g* for 5 min, followed by loading into a 3-ml syringe.

Rheological measurements

Rheology tests of the optoelectronically active ink and GelMA only (as a control) were performed using an HR-20 rheometer (TA Instruments, New Castle, DE, USA) with a 20-mm-diameter sand-blasted parallel plate, a Peltier steel plate, and a 500-μm plate-to-plate distance. The uncross-linked solutions for printing the GelMA and optoelectronically active ink were prepared as described earlier ($n = 3$). The solutions were stirred and transferred immediately to the plate of rheometer. First, we observed the temperature dependence of G' and G'' by conducting oscillation temperature sweeps at a constant shear strain of 5% in the frequency range of 0.1 to 100 rad/s. The temperature was decreased from 37° to 2°C at a cooling rate of 5°C/min, and 180 s of soaking time was set to keep temperature homogeneous throughout the hydrogels, which better reflected the physically cross-linked hydrogels that underwent a liquid to solid transition. The measurement of the viscosity of the hydrogels as a function of shear rate (0 to 100 s^{-1}) was conducted at 24°C after cooling them on the plate at 4°C for 5 min and recovery at 24°C for another 5 min.

Compression tests

Compression tests were performed using a 5966 series advanced electromechanical testing system with a 1-kN load cell (Instron, Norwood, MA, USA). Briefly, cross-linked cylinder-shaped samples (GelMA only and optoelectronically active ink) made using an EcoFlex mold with a 6-mm diameter and 2.5-mm thickness ($n = 5$) were compressed at a rate of 1.3 mm/min to 40% strain. The initial modulus (kPa) was calculated from the first 10% compression strain of the resulting curves.

Swelling and degradation

For both tests, cross-linked cylinder-shaped samples (GelMA only and optoelectronically active ink) with a 6-mm diameter and 2.5-mm thickness were made using an EcoFlex mold ($n = 4$). The samples for the degradation test were immediately immersed in DPBS at 37°C after cross-linking them, but the samples for the swelling test were lyophilized overnight before being immersed. To accelerate the degradation of the samples, collagenase type 4 (Worthington Biochemical Corporation, Lakewood, NJ, USA) was added to DPBS at a concentration of 190 collagen digestion units/ml. Afterward, at 30 min and 1, 2, 4, and 6 hours, the samples were taken out, rinsed, and lyophilized, and their dry weight was measured. For the swelling test, at the same time points as the degradation test, the samples were taken out and their wet weight was measured.

Absorption and impedance

For the absorption test, uncross-linked and cross-linked solutions of GelMA only and the optoelectronically active ink were used. Each uncross-linked solution was filled into a cuvette, and a UH4150 spectrometer (Hitachi High-Tech America Inc., Tokyo, Japan) was used to perform the ultraviolet-visible absorption measurement before and after cross-linking. The impedance of the cross-linked GelMA only and optoelectronically active ink was measured using a Multi/Autolab M204 electrochemical impedance analyzer (Metrohm AG, Riverview, FL, USA). A two-electrode configuration was used for each measurement.

Photocurrent characterization of μ-solar cells

Photocurrent characterization was performed using a patch-clamp setup (HEKA EPC-10 amplifier with the Patchmaster Next software, HEKA Elektronik, Lambrecht, Germany) integrated with an inverted microscope. A focused light spot was delivered using an M530L4-C5 collimated light-emitting diode (LED; Thorlabs Inc., Newton, NJ, USA) through the light path typically used for the eyepieces. The glass pipette was pulled in a P-97 micropipette puller (Sutter Instruments, Novato, CA, USA) with a resistance around 1 to 5 megohms. Voltage clamp mode was used to measure the photocurrent, which was extracted using a silver chloride electrode loaded in the glass pipette filled with DPBS mixed with a few μ-solar cells, uncross-linked GelMA only, or uncross-linked optoelectronically active bioink. After filling with any solutions containing μ-solar cells, the pipette tip typically had one μ-solar cell inside near the tip. During measurement, the pipette tip was first lowered into a DPBS bath, and the light was illuminated onto the tip (100-ms light pulses, 532 nm, and 2.8 mW/mm^2) through a 10x objective. For pipettes containing GelMA or the optoelectronically active bioink, the photocurrent measurements were taken before and after cross-linking using the parameters mentioned earlier. The data were analyzed and plotted using the MATLAB software (The MathWorks Inc., Natick, MA, USA).

Expansion and cardiac differentiation of hiPSCs

The hiPSCs (SCVI20) used in this study were kindly donated by the Stanford University Cardiovascular Institute Biobank, and the CMs generated in this study were obtained by differentiating the hiPSCs using the STEMdiff Cardiomyocyte Differentiation Kit (StemCell Technologies Inc., Vancouver, BC, Canada) as previously described (*35*). The cells were cultured and maintained in a feeder-free system of human embryonic stem cell-qualified Matrigel (Corning, Corning, NY, USA) and TeSR1 E8 (StemCell Technologies Inc., Vancouver, BC, Canada) under standard culture conditions (37°C at 5% CO_2). Briefly, 1×10^5 cells were plated in the TeSR E8 medium supplemented with Y-27632 (10 μM, StemCell Technologies Inc., Vancouver, BC, Canada). The medium was changed daily, and the cells were passaged using the cell dissociation recombinant enzymatic solution TrypLE Express (Gibco, Waltham, MA, USA). After the end of the differentiation protocol (day 15), the cells were harvested using the STEMdiff Cardiomyocyte Dissociation Kit (StemCell Technologies Inc., Vancouver, BC, Canada). The cells were washed two times with DPBS, and 1 ml of the Cardiomyocyte Dissociation Medium (37°C) was added per well. Culture plates were incubated for 15 min at 37°C and 5% CO_2. Afterward, the cells were dislodged by adding the Cardiomyocyte Support Medium and pipetting up and down 5 to 10 times. The cells were centrifuged at 300*g* for 5 min, and the pellet was resuspended in the Cardiomyocyte Support Medium to obtain hiPSC-CMs. Approximately 8×10^6 hiPSC-CMs/ml were used for each stimulation study. In addition to the hiPSC-CMs generated in this study, hiPSC-CMs (FUJIFILM Cellular Dynamics Inc., Madison, WI, USA) and rat neonatal CMs (Lonza, Basel, Switzerland) were also used to assess viabilities and morphological characteristics of CMs on the printed optoelectronically active scaffolds (described later).

Stimulation of hiPSC-CMs/rCMs with μ-solar cells

First, a small droplet of the μ-solar cell suspension was placed on the center of each MEA plate (60EcoMEA-Glass, Multichannel Systems MCS GmbH, Reutlingen, Germany) pretreated with fibronectin (1 mg/ml; Sigma-Aldrich, St. Louis, MO, USA). Next, the CMs were seeded onto the center of each MEA plate on top of the μ-solar cell layer. MEA plates with CMs in the absence of the μ-solar cells served as the control group. Finally, the plates were incubated and the media were changed daily until experimentation.

CMs cultured for 4 or 5 days were used to validate the μ-solar cells. The cardiac field potentials of the CMs were monitored by the multichannel system (MEA2100 Lite, MultiChannel Systems MCS GmbH, Reutlingen, Germany). An M530L4-C5 green LED light (Thorlabs Inc., Newton, NJ, USA) was passed through an amplifying lens to focus on the small spot atop the area containing the μ-solar cells to accelerate the beating of the CMs toward the targeted beating rate. The light and recording equipment were kept in an incubator to maintain the temperature and pH level throughout the entire experiment. Before stimulation, the CMs were allowed to stabilize for 10 min; afterward, their signals were recorded, and the spontaneous initial beating rate was determined. The targeted beating rates were chosen to be slightly higher than the spontaneous beating rate. A 4-min break was added after every 10 min of light stimulation to avoid any long-term light toxicity (*22*). The signals were recorded before stimulation (1 min), during stimulation (10 min), and after stimulation (1 min). This constitutes one round of stimulation and was repeated until the target frequency was reached. This cyclic light stimulation ensured the successful stimulation of the CM beating without introducing any side effects (*22*). Unless otherwise stated, all recorded signals from the MEAs were processed in MATLAB using a third-order Butterworth filter with a bandpass from 1 to 60 Hz. R-peak detection was performed using the R-DECO plugin (*36*) to determine the BPM over time.

Preparation of optoelectronically active cardiac scaffolds

After loading the optoelectronically active ink into syringes, they were stored in the fridge (4°C) for at least 20 min prior to use with the CELLINK BIO X (CELLINK, Gothenburg, Sweden) or the Allevi 2 (Allevi Inc., Philadelphia, PA, USA) printer. Conical nozzles of varying sizes (22, 25, and 27 Ga) were attached to the syringe although the final printing designs used 25-Ga nozzles. The printing speed was set to 1 to 2 mm/s, the nozzle temperature was 24° to 25°C, the bed temperature was 14°C, and the pressure was 5 to 20 kPa. Scaffolds for the viability and morphological assessments were made with dimensions of 10 mm by 10 mm by 0.5 mm ($L \times W \times H$). Scaffolds for the stimulation procedures were made with dimensions of 5 mm by 4.4 mm by 0.5 mm ($L \times W \times H$). After printing, the scaffolds were cross-linked using a 385-nm CS20K3 UV Curing LED System (Thorlabs Inc., Newton, NJ, USA) for 30 s with the light source placed ~7 cm (~45.8 W/cm^2) above each sample.

Viability of optoelectronically active cardiac scaffolds

For viability and morphological assessments, frozen hiPSC-CMs (FUJIFILM Cellular Dynamics Inc., Madison, WI, USA) were thawed at 37°C, added dropwise to 5 ml of an iCell cardiomyocyte plating medium (FUJIFILM Cellular Dynamics Inc., Madison, WI, USA) according to the instructions provided. The hiPSC-CM suspension was centrifuged at 1000 rpm for 5 min and resuspended in 200 μl of the iCell cardiomyocyte plating medium to obtain a cell suspension with 5×10^6 hiPSC-CMs. Each of the printed optoelectronically active scaffolds was seeded with 60 to 80 μl of the cell suspension and incubated at 37°C, in a cell incubator with 5% CO_2 and 95% humidity. After 24 hours of incubation, the plating medium was replaced with the iCell cardiomyocyte maintenance medium. The maintenance medium was refreshed every 48 hours.

Similarly, rCMs at ~80% confluency were washed with DPBS, trypsinized, and resuspended in rat cardiomyocyte growth medium (RCGM) to obtain an rCM-cell suspension at a concentration of 8×10^6 cells/ml. Next, 50 to 60 μl of the rCM-cell suspension was seeded onto the scaffold. The scaffolds were incubated at 37°C, in a cell incubator with 5% CO_2 and 95% humidity. After 12 hours, RCGM was replaced with RCGM containing 200 μM BrdU (5-bromo-2′-deoxyuridine) and was refreshed every 48 hours. Viability, morphology, and synchronized beating of both optoelectronically active cardiac scaffolds seeded with hiPSC-CMs or rCMs were evaluated as described below.

Viabilities of CMs on their respective optoelectronically active cardiac scaffolds were measured by the Live/Dead viability/cytotoxicity kit according to the manufacturer's instructions. Briefly, the cardiac scaffolds were washed twice with DPBS and placed in the wells of a 12-well plate, followed by the addition of live/dead staining solution containing 4 mM calcein acetoxymethyl (Calcein-AM) (1 μl/ml) and 2 mM ethidium homodimer-1 (2 μl/ml) in DPBS. After incubation at 37°C for 30 min, the scaffolds were washed three times with DPBS and imaged using an Eclipse Ti2 inverted microscope (Nikon, Melville, NY, USA). Percentages of viable CMs were determined using the ImageJ software.

Viability and staining assays

Using 1 ml of Accutase, the hiPSC-CMs were divided into single cells for 10 to 15 min. FlowBuffer-1 [DPBS with 0.5% bovine serum albumin (BSA)] was used to resuspend the hiPSC-CMs after which they were stained using the appropriate conjugated primary antibodies. A BD Accuri C6 Plus flow cytometer was used to acquire the data, and the FlowJo software was used to process it. For immunophenotyping by immunofluorescence, differentiated CMs attached to the RBOES were fixed with 4% paraformaldehyde and stained with 4′,6-diamidino-2-phenylindole (DAPI).

Morphological analyses and immunostaining of optoelectronically active cardiac scaffolds

For morphological analyses, Alexa Fluor 488–phalloidin or Alexa Fluor 549–phalloidin was used for F-actin staining. The optoelectronically active cardiac scaffolds were washed twice with DPBS and fixed with paraformaldehyde (4 vol % in DPBS) for 15 to 20 min. The scaffolds were then treated with Triton X-100 (0.2 vol % in DPBS) for 1 hour at room temperature. After gentle washing three times with DPBS, Alexa Fluor 488–phalloidin or Alexa Fluor 549–phalloidin (1:200 in 0.1 vol % BSA) was added to the scaffolds and incubated for 1 to 2 hours at room temperature. The samples were washed again with DPBS, and then nuclei were stained with DAPI for 5 min at room temperature. After washing three times with DPBS, fluorescence images were taken using a Zeiss LSM 880 confocal microscope (Carl Zeiss AG, NY, USA).

Moreover, the optoelectronically active cardiac scaffolds were assessed for expression of the cardiac cell specific markers by immunostaining. For this, the scaffolds were fixed with paraformaldehyde (4 vol % in DPBS) for 15 to 20 min at room temperature, permeabilized with Triton X-100 (0.2 vol % in DPBS) for 1 hour at room temperature, and then blocked with goat serum (5 vol % in DPBS) for 2 hours at room temperature. The scaffolds were then incubated overnight at 4°C with the primary antibodies, including sarcomeric α-actinin, connexin 43, cardiac troponin T, and cardiac troponin I antibodies (Abcam Limited, Waltham, MA, USA) at 1:200 dilution in a blocking buffer. The scaffolds were washed three times with DPBS and incubated overnight at 4°C with the relevant secondary antibody (Alexa Fluor 594–conjugated goat anti-rabbit secondary antibody or Alexa Fluor 488–conjugated goat anti-mouse secondary antibody) at 1:200 dilution in a blocking buffer. After washing with the scaffolds with DPBS, the nuclei were counterstained with DAPI and examined under the Zeiss LSM880 confocal microscope.

Stimulation of optoelectronically active scaffolds

The optoelectronically active scaffolds were first printed directly on the electrode areas of the MEA plates. The hiPSC-CMs were seeded at a concentration of 8×10^6 cells/ml onto the scaffolds in 25- to 30-μl droplets. The optoelectronically active scaffolds were left in the incubator until consistent beating was observed (after 3 to 5 days of incubation). The media were changed daily until experimentation. The same general stimulation protocol (round by round) was followed, and the MEA 2100 Lite system was used to collect data. The beating rates from the recorded ECG were determined using the R-DECO plugin, and the activation maps were created using MATLAB. The pre- and poststimulation BPMs were determined from a 10-s period in the recordings before and after each stimulation round.

Phototoxicity assay of the optoelectronically active scaffolds

The scaffolds used for this assay were stimulated for 7 days, ~1 hour/day using the stimulation protocol as described earlier (four rounds). The optoelectronically active scaffolds seeded with hiPSC-CMs were first placed in a collagenase type 4 (1 mg/ml; Worthington Biochemical Corporation, Lakewood, NJ, USA) solution to digest the hydrogel. The hiPSC-CMs were dissociated into single cells with 1 ml of Accutase for 10 to 15 min. The cells were resuspended in FlowBuffer-1 (DPBS with 0.5% BSA), and a drop of TO-PRO3 Ready Flow Reagent live/dead cell stain (Invitrogen, Waltham, MA, USA) was added. After incubating the samples in the dark for 5 to 10 min, results were obtained with a BD Accuri C6 Plus flow cytometer (Becton, Dickinson and Company, Franklin Lakes, NJ, USA) and processed using the FlowJo software.

ECG waveform parameter calculations and statistical analysis

To analyze the ECG signal, the raw data were first preprocessed and segmented into individual beats. The mean ECG signal was calculated across all channels, and R-peaks were detected with a minimum peak height threshold set at 2 SDs above the mean and a minimum peak distance of 0.6 s to avoid detecting multiple peaks within a single heartbeat. Each beat was extracted into segments using a window centered on the R-peak location, with a total segment length of 2000 data points (1 s at a sampling frequency of 2000 Hz). For each beat and channel, the extracted signal was filtered using a 50^{th}-order low-pass finite impulse response filter with a cutoff frequency of 100 Hz, designed using a Hamming window. This filtering step removed high-frequency noise without phase distortion by applying the filter in both forward and reverse directions. A moving average filter with a window size of 100 data points was subsequently applied to further smooth the signal to clearly identify the QRS locations. QRS durations were calculated by identifying the Q and S points surrounding each R-peak. A search window of 0.1 s before the R-peak was used to detect the Q point, and a 0.2-s window after the R-peak was used to detect the S point. The QRS duration was computed as the time difference between the identified Q and S points. This process was repeated for each detected R-peak across all beats and channels. For the calculation of QR and RS slopes, the difference in signal amplitude between the R-peak and Q point, and the R-peak and S point, was computed. The QR slope was defined as the change in amplitude between the Q point and the R-peak, divided by the time between these two points. Similarly, the RS slope was computed as the change in amplitude between the R-peak and the S point, divided by the time between them. The slopes were averaged across all detected beats for each channel. The peak-to-peak amplitude for each beat was computed by taking the difference between the maximum and minimum values of the signal within each segment. This calculation was performed for each beat and across all channels, with the peak-to-peak amplitudes averaged per channel.

We conducted a statistical analysis to compare the RS slope, QR slope, QRS duration, and peak-to-peak amplitude features before and after stimulation using paired *t* tests for each channel. The mean *P* values for RS slope, QR slope, QRS duration, and peak-to-peak amplitude were 0.5485, 0.6406, 0.5867, and 0.6018, respectively. In all cases, the *P* values were greater than 0.05, indicating that the differences between the two groups were not statistically significant. The standard error of the mean (SEM) was also calculated, with values ranging from 0.0074 to 4.0504, further supporting the lack of significant variation between the groups.

Stimulation of rat heart with the optoelectronically active scaffolds

The optoelectronically active scaffolds (same dimensions as used for in vitro stimulation) were printed onto tissue culture-treated petri dishes and then seeded with rCMs (8×10^6 cells/ml). After 5 days of seeding, the scaffolds were then used for the in vivo experiment. After the rat was placed under anesthesia, the chest was opened to expose the heart. The scaffold was laminated on the epicardial surface of the rat heart after sprinkling a small amount of Transglutaminase (Modernist Pantry LLC, Eliot, ME, USA) powder onto the side that would contact the heart. A green LED light (Thorlabs Inc., Newton, NJ, USA) was passed through an amplifying lens to focus on the optoelectronically active scaffold. The target stimulation rate was set to ~5 Hz (40-ms pulse duration) with a function generator. The stimulation period began after 1 min of recording the spontaneous beating rate and was stopped when the target beating rate was reached. The Mouse Monitor (Indus Instruments, Webster, TX, USA) was used to capture the ECG signals from the body of the rat. The beating rates from the recorded ECG were determined using the R-DECO plugin in MATLAB. Temperature measurements were captured using an FLIR ONE Gen 3 Professional Thermal Camera (Teledyne FLIR LLC, Wilsonville, OR, USA). The animals in this study were handled and maintained per the requirements of the Laboratory Animal Welfare Act (P.L. 89-544) and its 1970 (P.L. 91-579), 1976 (P.L. 94-279), and 1985 (P.L. 99-198) amendments and within the specifications indicated below. Compliance was accomplished by conforming to the standards in the Guide for the Care and the Use of Laboratory Animals, ILAR, National Academy Press, revised 2011, and all procedures were approved by the Texas Heart Institute Institutional Animal Care and Use Committee (#2023-02).

Supplementary Materials

The PDF file includes:
Figs. S1 to S16
Legends for movies S1 to S4

Other Supplementary Material for this manuscript includes the following:
Movies S1 to S4

REFERENCES AND NOTES

1. M. Yadid, H. Oved, E. Silberman, T. Dvir, Bioengineering approaches to treat the failing heart: From cell biology to 3D printing. *Nat. Rev. Cardiol.* **19**, 83–99 (2022).
2. L. Wang, Y. Liu, G. Ye, Y. He, B. Li, Y. Guan, B. Gong, K. Mequanint, M. M. Q. Xing, X. Qiu, Injectable and conductive cardiac patches repair infarcted myocardium in rats and minipigs. *Nat. Biomed. Eng.* **5**, 1157–1173 (2021).
3. B. Duan, State-of-the-art review of 3D bioprinting for cardiovascular tissue engineering. *Ann. Biomed. Eng.* **45**, 195–209 (2017).
4. A. Lee, A. R. Hudson, D. J. Shiwarski, J. W. Tashman, T. J. Hinton, S. Yerneni, J. M. Bliley, P. G. Campbell, A. W. Feinberg, 3D bioprinting of collagen to rebuild components of the human heart. *Science* **365**, 482–487 (2019).
5. S. R. Shin, C. Zihlmann, M. Akbari, P. Assawes, L. Cheung, K. Zhang, V. Manoharan, Y. S. Zhang, M. Yuksekkaya, K. T. Wan, M. Nikkhah, M. R. Dokmeci, X. S. Tang, A. Khademhosseini, Reduced graphene oxide-GelMA hybrid hydrogels as scaffolds for cardiac tissue engineering. *Small* **12**, 3677–3689 (2016).
6. B. Lu, M. Ye, J. Xia, Z. Zhang, Z. Xiong, T. Zhang, Electrical stimulation promotes the vascularization and functionalization of an engineered biomimetic human cardiac tissue. *Adv. Healthc. Mater.* **12**, e2300607 (2023).
7. M. Radisic, H. Park, H. Shing, T. Consi, F. J. Schoen, R. Langer, L. E. Freed, G. Vunjak-Novakovic, Functional assembly of engineered myocardium by electrical stimulation of cardiac myocytes cultured on scaffolds. *Proc. Natl. Acad. Sci. U.S.A.* **101**, 18129–18134 (2004).
8. N. Tandon, C. Cannizzaro, P.-H. G. Chao, R. Maidhof, A. Marsano, H. T. H. Au, M. Radisic, G. Vunjak-Novakovic, Electrical stimulation systems for cardiac tissue engineering. *Nat. Protoc.* **4**, 155–173 (2009).
9. S. S. Nunes, J. W. Miklas, J. Liu, R. Aschar-Sobbi, Y. Xiao, B. Zhang, J. Jiang, S. Masse, M. Gagliardi, A. Hsieh, N. Thavandiran, M. A. Laflamme, K. Nanthakumar, G. J. Gross, P. H. Backx, G. Keller, M. Radisic, Biowire: A platform for maturation of human pluripotent stem cell-derived cardiomyocytes. *Nat. Methods* **10**, 781–787 (2013).
10. J. Hopkins, L. Travaglini, A. Lauto, T. Cramer, B. Fraboni, J. Seidel, D. Mawad, Photoactive organic substrates for cell stimulation: Progress and perspectives. *Adv. Mater. Technol.* **4**, 1800744 (2019).
11. S. F. Cogan, K. A. Ludwig, C. G. Welle, P. Takmakov, Tissue damage thresholds during therapeutic electrical stimulation. *J. Neural Eng.* **13**, 021001 (2016).
12. J. C. Williams, E. Entcheva, Optogenetic versus electrical stimulation of human cardiomyocytes: Modeling insights. *Biophys. J.* **108**, 1934–1945 (2015).
13. A. Moreno, R. D. Walton, M. Constantin, O. Bernus, E. J. Vigmond, J. D. Bayer, Wide-area low-energy surface stimulation of large mammalian ventricular tissue. *Sci. Rep.* **9**, 15863 (2019).
14. F. Gilbert, A. R. Harris, R. M. I. Kapsa, Controlling brain cells with light: Ethical considerations for optogenetic clinical trials. *AJOB Neurosci.* **5**, 3–11 (2014).
15. P. Kerscher, J. A. Kaczmarek, S. E. Head, M. E. Ellis, W. J. Seeto, J. Kim, S. Bhattacharya, V. Suppiramaniam, E. A. Lipke, Direct production of human cardiac tissues by pluripotent stem cell encapsulation in gelatin methacryloyl. *ACS Biomater. Sci. Eng.* **3**, 1499–1509 (2016).
16. K. Zhu, S. R. Shin, T. van Kempen, Y. C. Li, V. Ponraj, A. Nasajpour, S. Mandla, N. Hu, X. Liu, J. Leijten, Y. D. Lin, M. A. Hussain, Y. S. Zhang, A. Tamayol, A. Khademhosseini, Gold nanocomposite bioink for printing 3D cardiac constructs. *Adv. Funct. Mater.* **27**, (2017).
17. G. Ying, N. Jiang, C. Yu, Y. S. Zhang, Three-dimensional bioprinting of gelatin methacryloyl (GelMA). *Biodes. Manuf.* **1**, 215–224 (2018).
18. D. Bejleri, B. W. Streeter, A. L. Y. Nachlas, M. E. Brown, R. Gaetani, K. L. Christman, M. E. Davis, A bioprinted cardiac patch composed of cardiac-specific extracellular matrix and progenitor cells for heart repair. *Adv. Healthc. Mater.* **7**, e1800672 (2018).
19. S. K. Kang, S. W. Hwang, H. Cheng, S. Yu, B. H. Kim, J. H. Kim, Y. Huang, J. A. Rogers, Dissolution behaviors and applications of silicon oxides and nitrides in transient electronics. *Adv. Funct. Mater.* **24**, 4427–4434 (2014).
20. Y. Jiang, X. Li, B. Liu, J. Yi, Y. Fang, F. Shi, X. Gao, E. Sudzilovsky, R. Parameswaran, K. Koehler, V. Nair, J. Yue, K. Guo, Y. Fang, H.-M. Tsai, G. Freyermuth, R. C. S. Wong, C.-M. Kao, C.-T. Chen, A. W. Nicholls, X. Wu, G. M. G. Shepherd, B. Tian, Rational design of silicon structures for optically controlled multiscale biointerfaces. *Nat. Biomed. Eng.* **2**, 508–521 (2018).
21. S. Yu, W. Yue, T. Guo, Y. Liu, Y. Zhang, S. Khademi, T. Zhou, Z. Xu, B. Song, T. Wu, F. Liu, Y. Tai, X. Yu, H. Wang, The effect of the subthreshold oscillation induced by the neurons'

resonance upon the electrical stimulation-dependent instability. *Front. Neurosci.* **17**, 1178606 (2023).

22. R. Parameswaran, K. Koehler, M. Y. Rotenberg, M. J. Burke, J. Kim, K.-Y. Jeong, B. Hissa, M. D. Paul, K. Moreno, N. Sarma, T. Hayes, E. Sudzilovsky, H.-G. Park, B. Tian, Optical stimulation of cardiac cells with a polymer-supported silicon nanowire matrix. *Proc. Natl. Acad. Sci. U.S.A.* **116**, 413–421 (2019).
23. Y. Fang, A. Prominski, M. Y. Rotenberg, L. Meng, H. Acaron Ledesma, Y. Lv, J. Yue, E. Schaumann, J. Jeong, N. Yamamoto, Y. Jiang, B. Elbaz, W. Wei, B. Tian, Micelle-enabled self-assembly of porous and monolithic carbon membranes for bioelectronic interfaces. *Nat. Nanotechnol.* **16**, 206–213 (2021).
24. P. Li, J. Zhang, H. Hayashi, J. Yue, W. Li, C. Yang, C. Sun, J. Shi, J. Huberman-Shlaes, N. Hibino, B. Tian, Monolithic silicon for high spatiotemporal translational photostimulation. *Nature* **626**, 990–998 (2024).
25. K. Kim, S. J. Yoo, S. Y. Kim, T. Lee, S. H. Lim, J. E. Jang, M. Je, C. Moon, J. W. Choi, Subthreshold electrical stimulation as a low power electrical treatment for stroke rehabilitation. *Sci. Rep.* **11**, 14048 (2021).
26. V. Biasci, L. Santini, G. A. Marchal, S. Hussaini, C. Ferrantini, R. Coppini, L. M. Loew, S. Luther, M. Campione, C. Poggesi, F. S. Pavone, E. Cerbai, G. Bub, L. Sacconi, Optogenetic manipulation of cardiac electrical dynamics using sub-threshold illumination: Dissecting the role of cardiac alternans in terminating rapid rhythms. *Basic Res. Cardiol.* **117**, 25 (2022).
27. S. H. Sunwoo, M. J. Cha, S. I. Han, H. Kang, Y. S. Cho, D. H. Yeom, C. S. Park, N. K. Park, S. W. Choi, S. J. Kim, G. D. Cha, D. Jung, S. Choi, S. Oh, G. B. Nam, T. Hyeon, D. H. Kim, S. P. Lee, Ventricular tachyarrhythmia treatment and prevention by subthreshold stimulation with stretchable epicardial multichannel electrode array. *Sci. Adv.* **9**, eadf6856 (2023).
28. M. Silvera Ejneby, M. Jakesova, J. J. Ferrero, L. Migliaccio, I. Sahalianov, Z. Zhao, M. Berggren, D. Khodagholy, V. Derek, J. N. Gelinas, E. D. Glowacki, Chronic electrical stimulation of peripheral nerves via deep-red light transduced by an implanted organic photocapacitor. *Nat. Biomed Eng.* **6**, 741–753 (2022).
29. X. Wu, Y. Jiang, N. J. Rommelfanger, F. Yang, Q. Zhou, R. Yin, J. Liu, S. Cai, W. Ren, A. Shin, K. S. Ong, K. Pu, G. Hong, Tether-free photothermal deep-brain stimulation in freely behaving mice via wide-field illumination in the near-infrared-II window. *Nat. Biomed. Eng.* **6**, 754–770 (2022).
30. Z. Ou, Y. S. Duh, N. J. Rommelfanger, C. H. C. Keck, S. Jiang, K. Brinson Jr., S. Zhao, E. L. Schmidt, X. Wu, F. Yang, B. Cai, H. Cui, W. Qi, S. Wu, A. Tantry, R. Roth, J. Ding, X. Chen, J. A. Kaltschmidt, M. L. Brongersma, G. Hong, Achieving optical transparency in live animals with absorbing molecules. *Science* **385**, eadm6869 (2024).
31. P. Avci, A. Gupta, M. Sadasivam, D. Vecchio, Z. Pam, N. Pam, M. R. Hamblin, Low-level laser (light) therapy (LLLT) in skin: Stimulating, healing, restoring. *Semin. Cutan. Med. Surg.* **32**, 41–52 (2013).
32. Z. Rao, Y. Lu, Z. Li, K. Sim, Z. Ma, J. Xiao, C. Yu, Curvy, shape-adaptive imagers based on printed optoelectronic pixels with a kirigami design. *Nat. Electron.* **4**, 513–521 (2021).
33. K. Sim, S. Chen, Z. Li, Z. Rao, J. Liu, Y. Lu, S. Jang, F. Ershad, J. Chen, J. Xiao, C. Yu, Three-dimensional curvy electronics created using conformal additive stamp printing. *Nat. Electron.* **2**, 471–479 (2019).
34. D. Wang, S. Maharjan, X. Kuang, Z. Wang, L. S. Mille, M. Tao, P. Yu, X. Cao, L. Lian, L. Lv, J. J. He, G. Tang, H. Yuk, C. K. Ozaki, X. Zhao, Y. S. Zhang, Microfluidic bioprinting of tough hydrogel-based vascular conduits for functional blood vessels. *Sci. Adv.* **8**, eabq6900 (2022).
35. F. C. Mesquita, J. Morrissey, P. F. Lee, G. Monnerat, Y. Xi, H. Andersson, F. C. Nogueira, G. B. Domont, L. C. Sampaio, C. Hochman-Mendez, D. A. Taylor, Cues from human atrial extracellular matrix enrich the atrial differentiation of human induced pluripotent stem cell-derived cardiomyocytes. *Biomater. Sci.* **9**, 3737–3749 (2021).
36. J. Moeyersons, M. Amoni, S. Van Huffel, R. Willems, C. Varon, R-DECO: An open-source Matlab based graphical user interface for the detection and correction of R-peaks. *PeerJ Comput. Sci.* **5**, e226 (2019).

Acknowledgments: We thank the Texas Heart Institute Cardiovascular Research Laboratories for contribution to the porcine tissue sharing resource and G. Costas for the animal care and welfare. **Funding:** C.Y. and Y.S.Z. would like to acknowledge the funding support by the National Institutes of Health (R21EB026175 and R21EB030257). C.Y. would also like to acknowledge the funding support by the National Science Foundation (CBET-2227063). Y.S.Z. would also like to acknowledge the support from the National Institutes of Health (R21HL168656, R00CA201603, R01EB028143, R01HL166522, R56EB034702, and R01CA282451), the National Science Foundation (CBET-EBMS-1936105 and CISE-IIS-2225698), the American Heart Association (19TPA34850188), the Chan Zuckerberg Initiative (2022-316712), and the Brigham Research Institute. **Author contributions:** F.E., Z.R., Y.S.Z., and C.Y. conceived the concept. F.E. and Z.R. initiated and led the whole project. F.E., Z.R., S.M., J.H., L.G., S.J., Y.L., S.P., X.W., and Y.T. prepared the materials and/or fabricated the devices. F.E., Z.R., S.M., F.C.P.M., J.H., T.H., Y.W., X.W., Y.T., J.W., C.E.G.-M., and L.C.O.C. contributed to the material and in vitro characterization. F.E., Z.R., F.C.P.M., E.C.d.C., A.M.-R., A.E., and C.H.-M. performed the animal experiments. F.E., Z.R., S.M., J.H., M.Z., X.L.L., Y.S.Z., and C.Y. analyzed the experimental data. F.E., Z.R., and S.M. prepared the manuscript. F.E., Z.R., S.M., J.Y., Y.S.Z., and C.Y. revised the manuscript. All authors reviewed and approved the manuscript. **Competing interests:** Y.S.Z. consulted for Allevi by 3D Systems and sits on the scientific advisory board and holds options of Xellar, neither of which, however, participated in or biased the work. The relevant interests are managed by the Brigham and Women's Hospital. The other authors declare that they have no competing interests. **Data and materials availability:** All data needed to evaluate the conclusions in the paper are present in the paper and/or the Supplementary Materials.

Submitted 9 October 2024
Accepted 23 December 2024
Published 24 January 2025
10.1126/sciadv.adt7210

Science Advances

Bioprinted optoelectronically active cardiac tissues

Faheem Ershad, Zhoulyu Rao, Sushila Maharajan, Fernanda C. Paccola Mesquita, Junkyu Ha, Lei Gonzalez, Tahir Haideri, Ernesto Curty da Costa, Angel Moctezuma-Ramirez, Yuqi Wang, Seonmin Jang, Yuntao Lu, Shubham Patel, Xiaoyang Wang, Yifan Tao, Joshua Weygant, Carlos Ezio Garciamendez-Mijares, Luis Carlos Orrantia Clark, Muhammad Zubair, Xiaojun Lance Lian, Abdelmotagaly Elgalad, Jian Yang, Camila Hochman-Mendez, Yu Shrike Zhang, and Cunjiang Yu

Sci. Adv. **11** (4), eadt7210. DOI: 10.1126/sciadv.adt7210

Science Advances (ISSN 2375-2548) is published by the American Association for the Advancement of Science. 1200 New York Avenue NW, Washington, DC 20005. The title *Science Advances* is a registered trademark of AAAS.